# Impact of Cathode Ring Busbars on Potshell Temperature by Radiation Heat Transfer

**André Felipe Schneider[1], Daniel Richard[2], Vinko Potočnik[3] and Marc Dupuis[4]**
1. Consultant
2. Associate
Center of Excellence for Aluminum, Hatch, Montréal, Canada
3. Consultant
Vinko Potocnik Consultant, Saguenay, Canada
4. Consultant
GeniSIM, Saguenay, Canada
Corresponding author: andre.schneider@hatch.com
https://doi.org/10.71659/icsoba2024-al053

**Abstract**

Cell energy balance is typically treated independently from both magnetohydrodynamics (MHD) and pot-to-pot busbar design, even though all three aspects are intertwined in many ways. Of particular interest is the fact that the downstream (DS) sidewall of typical side-by-side, side riser reduction cells is usually hotter than in the upstream (US), suggesting that the MHD behavior impacts the distribution of heat losses around the shell. This has been investigated by different authors and it was found that the flow of the liquid metal and bath, the reduction of anode slot depth with anode block consumption and the metal pad heaving all contribute to the asymmetry of the potshell temperature distribution. Moreover, during the 41st International ICSOBA Conference in 2023, it was suggested that hotter DS cathode busbars would also contribute to the hotter DS sidewalls observed in actual practice; specifically, the DS busbars are hotter because they have smaller cross-section as the means of balancing the US-to-DS current split. To address this intriguing assertion, this work investigates the radiation heat transfer between cathode ring busbar and potshell, which has not been included in the past models. The radiation heat transfer between the potshell, pot-to-pot busbars and ambient was implemented in the modernized ANSYS-based cell energy balance model presented earlier [1–3]. Key conclusions are illustrated by means of numerical results obtained for a fictitious 375 kA reduction cell.

**Keywords:** Aluminum reduction cells, Energy balance, Busbars, Potshell temperature, Thermal radiation.

## 1. Introduction

As pointed out in a previous paper [3], the operational window of an aluminum reduction cell is largely determined by magnetohydrodynamics (MHD) and energy balance. While these two fundamental aspects of cell design are usually studied independently, they are in fact coupled. The ledge profile affects the internal electrical current distribution – and, ultimately, Lorentz forces – while MHD impacts both the metal pad heave and the flow pattern of the liquid phases. These interactions are commonly neglected in numerical modeling thus enabling the employment of pure, stand-alone thermoelectrical (TE) numerical analyses to study the energy balance of a Hall-Héroult cell. Such modeling approaches [1–2, 4–8] often ignore the local effects of metal pad velocity, alumina concentration, bubble-driven flow and metal pad heaving (amongst other phenomena) on the heat transfer between the liquid phases and the ledge.

However, actual practice shows that the downstream (DS) sidewall of typical side-by-side, side riser reduction cells is usually hotter than in the upstream (US), suggesting that the MHD behavior impacts the distribution of heat losses around the shell – see Figure 1.

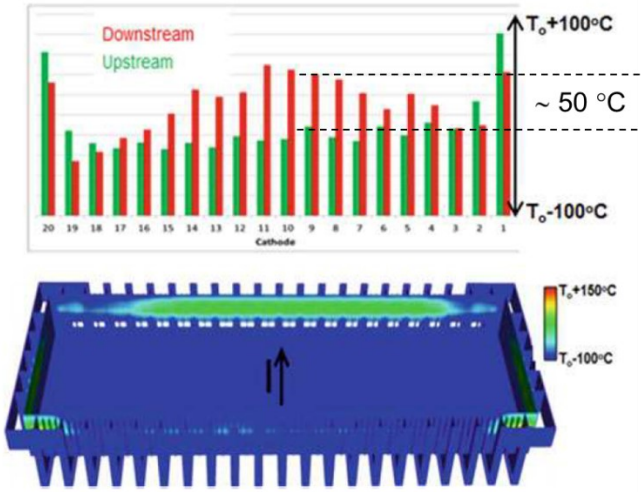


**Figure 1. Sidewall temperature distribution above collector bars for an AP4X cell, where potline current flows from the bottom to the top of the page – adapted from [9]. Top: measurements. Bottom: numerical predictions.**

Considerable efforts have been made by different authors [3, 9–13] to better account for the effects of the liquid phases flow on the energy balance of a reduction cell. For instance, Langlois *et al*. (2015) [10] introduced a coupled MHD-TE model that considers the MHD-induced flow while ignoring the bubble-driven effects on the bath, the thermal effects caused by alumina dissolution and the metal pad-bath interface deformation. Application [11] of this validated approach [9] to the AP44 reduction technology installed at the Rio Tinto Alma smelter indicates that metal pad flow regions with high velocity magnitudes correlate (to some extent) with hot potshell regions – compare, for instance, the hot headwalls and US corners found in Figure 1 against the high velocity vectors in the same locations in Figure 2. Notice, however, that the flow velocity magnitude on its own cannot explain the hot central region of the DS sidewall found in this same work.

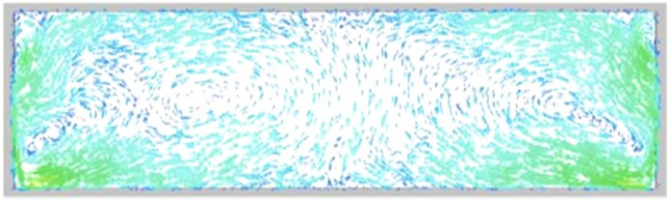

**Figure 2. Predicted liquids velocity field for an AP44 cell (scale not shown), where potline current flows from the bottom to the top of the page – adapted from [10].**

Bugnion and Kaenel (2023) [12] showed that directionality of the flow is also important as heat advection within the liquid phases – *i.e.*, the heating (or cooling) of a portion of bath or metal as it follows a given streamline – contributes to a non-uniform distribution of thermal power to be dissipated along the shell perimeter thus leading to uneven ledge profiles and, consequently, potshell temperature distributions. It is worth noticing that the relevance of heat advection was also pointed out by [9].

Modeling and experimental work by Chailly and coworkers (2023) [13] suggests that the evolution of the gas bubbles-induced recirculation of bath within the lateral channels as a function of anode service life may be responsible for local cyclic melting and forming of ledge and, therefore, temporal variations in measured sidewall temperature. The combined effect of the

consumed shape of the anode blocks and the anode slots directs the gas bubbles towards the DS side channel, creating a region of strong recirculation – see Figure 3.

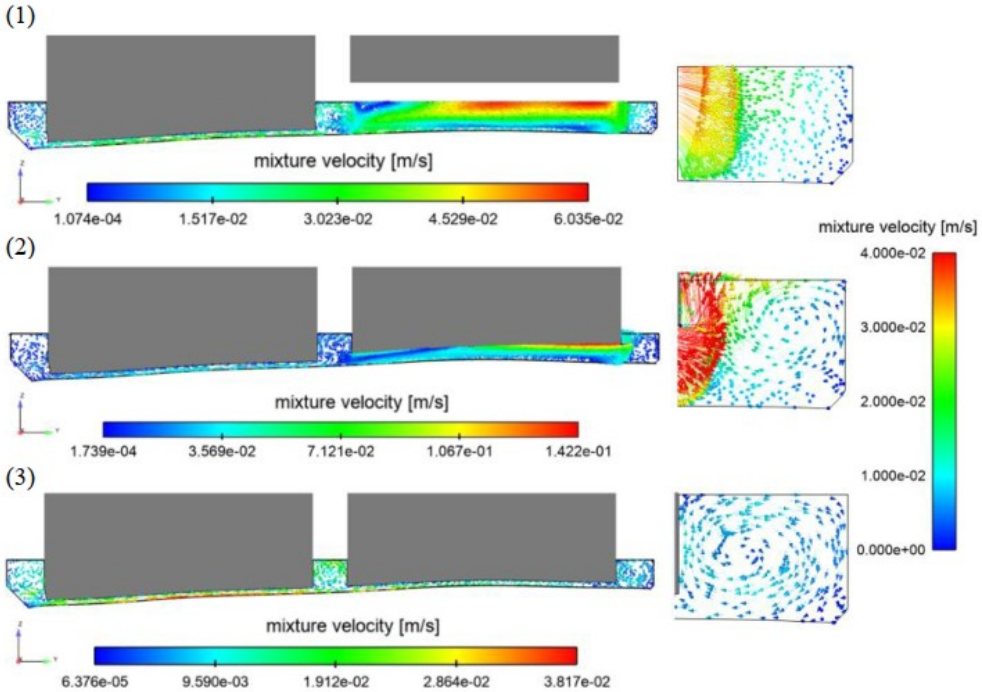


**Figure 3. Evolution of bath mixture velocity within the DS side channel of an AP30 cell as a function of anode service life, where potline current flows from left to right – reproduced from [13]. Top: immediately after anode replacement. Center: partially consumed anode with completely immersed slots. Bottom: end of anode service, once the slots are consumed.**

Metal pad heaving also impacts potshell temperature distribution, as previously shown [3] by the authors – refer to Figure 4. Given that heat fluxes at the lower ledge (facing metal) are systematically larger that those found at the upper ledge (facing bath), the higher metal pad-bath interface at the shell DS leads necessarily to a larger amount of thermal power being lost through that sidewall when compared to the US one, where said interface is at a lower position. It is also worth noticing that similar results were reported by [12].

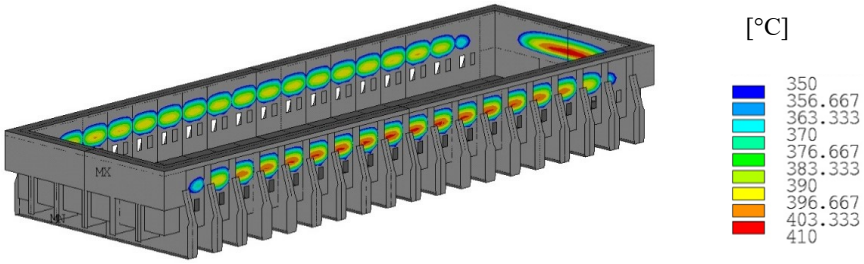


**Figure 4. Predicted potshell temperature distribution for a fictitious side-by-side, side riser reduction technology while considering the metal pad heave – reproduced from [3].**

Finally, during the 41st International ICSOBA Conference in 2023, it was suggested that DS cathode busbars – which are typically hotter than their US counterparts in typical side-by-side, side riser pots (Figure 5) – would also contribute to the hotter DS sidewalls. To address this intriguing assertion, this work investigates the radiation heat transfer between cathode ring busbar and potshell, which has not been included in the past models [1–3].

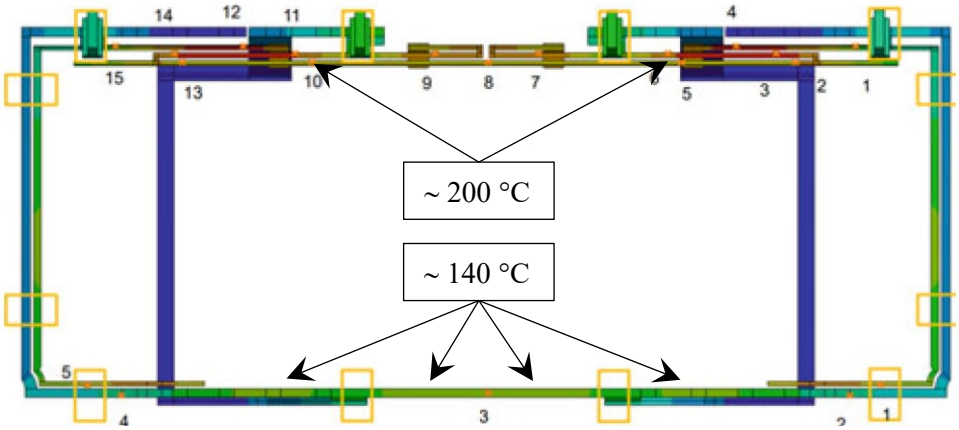


**Figure 5. Predicted busbar temperature distribution for a DX cell at 420 kA in the EGA Al Taweelah smelter, where potline current flows from the bottom to the top of the page – adapted from [14].**

## 2. Potshell Heat Losses and The Radiosity Method

Consider the typical cell cross-section found in Figure 6 and the potshell slice seen in Figure 7, where the location of the metal pad-bath interface is denoted by the ledge trench. The cell internal heat is conducted through the anode assemblies, the crust, the ledge, the lining, the cathode assemblies and the potshell. At the control volume boundaries, heat is lost to the surroundings by different mechanisms acting in parallel.

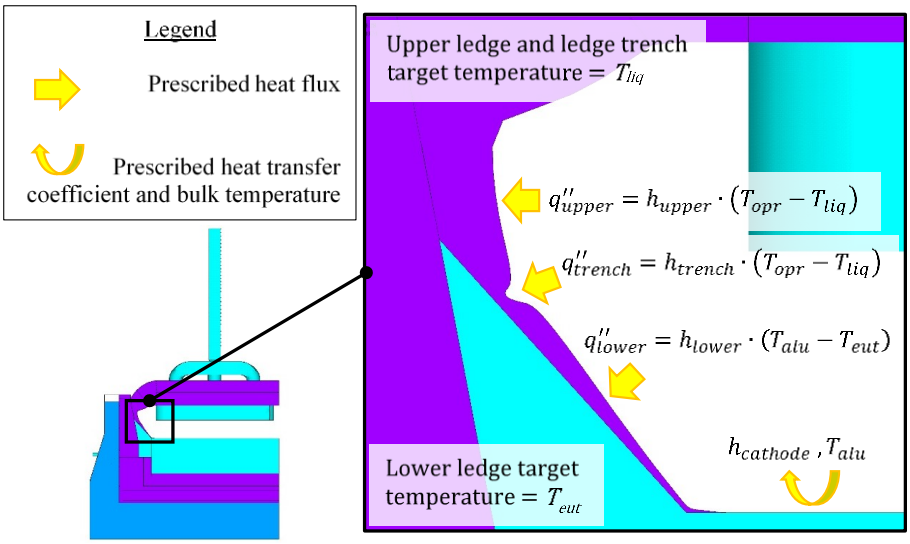


**Figure 6. Typical cross-section of an aluminum reduction cell – reproduced from [2].**

where:

| | |
|---|---|
| $q''_{upper}$ | Prescribed heat flux at the upper ledge (facing bath), W/m$^2$ |
| $h_{upper}$ | Uniform heat transfer coefficient at the upper ledge (facing bath), W/m$^2$ °C |
| $T_{opr}$ | Bulk bath temperature, °C |
| $T_{liq}$ | Liquidus temperature evaluated at the bulk bath composition, °C |
| $q''_{trench}$ | Prescribed heat flux at the trench region, W/m$^2$ |
| $h_{trench}$ | Parabolic heat transfer coefficient distribution that varies with the trench height, W/m$^2$ °C |

| | |
|---|---|
| $q''_{lower}$ | Prescribed heat flux at the lower ledge (facing metal), W/m$^2$ |
| $h_{lower}$ | Uniform heat transfer coefficient at the lower ledge (facing metal), W/m$^2$ °C |
| $T_{alu}$ | Bulk metal pad temperature, °C |
| $T_{eut}$ | Eutectic point evaluated at the bath film composition (facing metal), °C |
| $h_{cathode}$ | Prescribed uniform heat transfer coefficient at the cathode panel surface, W/m$^2$ °C. |

Despite the existing capability of controlling the amount of heat extracted from a Hall-Héroult cell by means of sophisticated heat exchanger technologies [15, 16], a potshell in most smelters typically exchanges thermal power with its surroundings by means of both convection in air and radiation mechanisms. These mechanisms are illustrated on a shell slice in Figure 7, where the numbers identify selected segments of an opened (or "leaky") radiation enclosure with two symmetry planes (used for computation of view factors and radiation heat exchange between different surfaces, including environment), and where the black dotted line above the collector bars represent a path for the averaging of the hot sidewall temperature that will be used in the analysis of the results later. Notice that, for the sake of clarity, only the busbar surfaces seeing the potshell are shown.

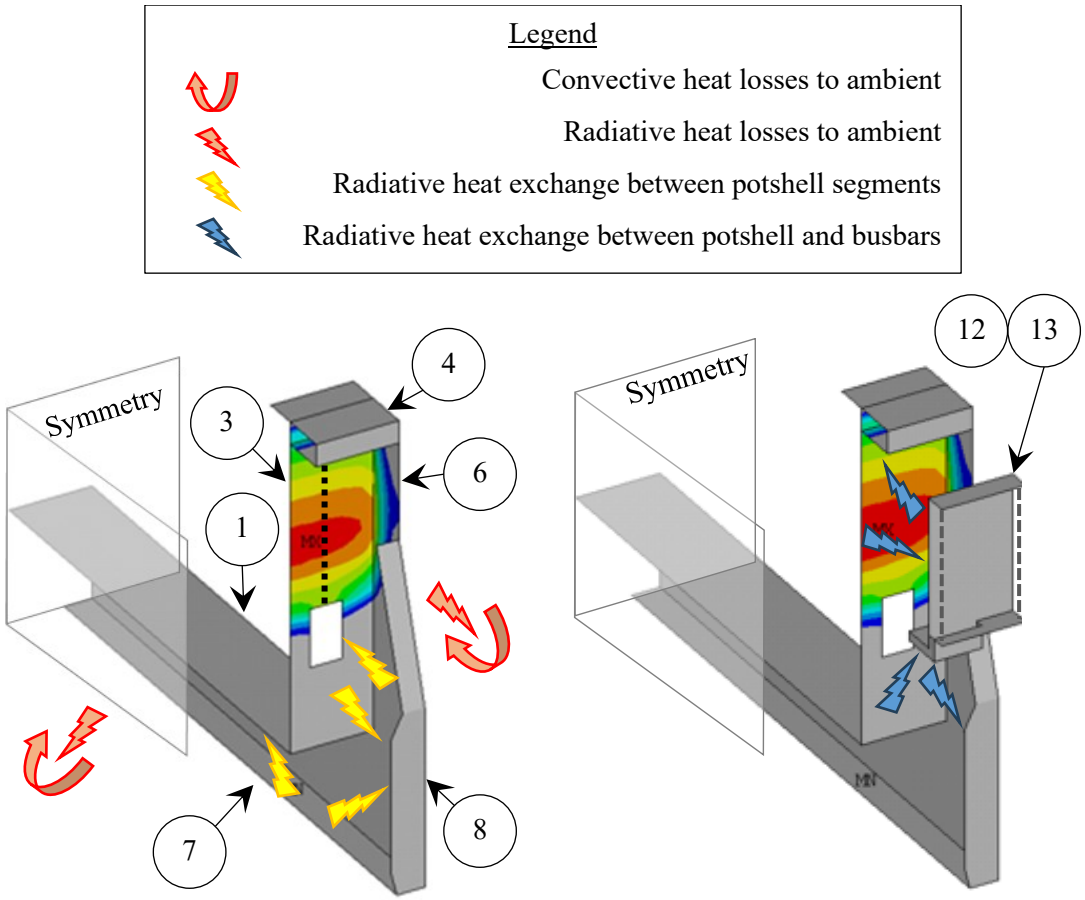


**Figure 7. Potshell heat transfer mechanisms illustrated on a typical cell slice. Left: heat losses to ambient and radiation heat exchange between different shell segments. Right: radiation heat exchange between potshell and cathode ring busbars.**

It can be readily seen upon inspection of both Equation (1) and Figure 7 that any given shell segment exchanges heat by means of radiation not only with the environment but also with other surfaces within its field of vision (including itself, should surface $i$ be concave).

$$q_{tot,i} = q_{conv,i} + \sum_{j=1}^{n} q_{rad,ij} \quad (1)$$

where:

| | |
|---|---|
| $q_{tot,i}$ | Total heat losses at surface $i$, W |
| $q_{conv,i}$ | Convection heat losses at surface $i$, W |
| $q_{rad,ij}$ | Net radiation heat exchange between surfaces $i$ and $j$, W. |

Radiation heat transfer between surfaces is a complex, highly non-linear phenomenon that is usually simplified in cell heat balance modeling by ignoring the radiation exchange between surfaces, such that only net radiation losses to the ambient are considered. This results in an equivalent heat transfer coefficient that conveniently includes both shell-to-ambient convection and shell-to-ambient thermal radiation phenomena, as per Equation (2).

$$h_{eqv,i} = h_{conv,i} + h_{rad,i} = h_{conv,i} + \left[ F_{iamb} \cdot \varepsilon_i \cdot \sigma \cdot \frac{\left( {T_i}^4 - {T_{rad,amb}}^4 \right)}{(T_i - T_{bulk})} \right] \quad (2)$$

where:

| | |
|---|---|
| $h_{eqv,i}$ | Equivalent (*i.e.*, convective and radiative) heat transfer coefficient between surface $i$ and ambient, W/m$^2$ K |
| $h_{conv,i}$ | Convection heat transfer coefficient at surface $i$, W/m$^2$ K |
| $h_{rad,i}$ | Radiation heat transfer coefficient at surface $i$, W/m$^2$ K |
| $F_{iamb}$ | Surface $i$-to-ambient view factor, dimensionless |
| $\varepsilon_i$ | Surface $i$ emissivity, dimensionless |
| $\sigma$ | Stefan-Boltzmann constant, 5.669×10$^{-8}$ W/m$^2$ K$^4$ |
| $T_i$ | Surface $i$ temperature, K |
| $T_{rad,amb}$ | Radiative ambient temperature, K |
| $T_{bulk}$ | Convective bulk temperature, K. |

The radiative ambient temperature $T_{rad,amb}$ is then used as one of the calibration parameters for shell heat losses and shell temperatures. Heat transfer coefficients between bath and freeze and metal and freeze are also adjusted to reproduce measured ledge profile.

When using Equation (2), the key assumption is that $F_{iamb} = 1$ to comply with the view factor summation rule in Equation (3).

$$\sum_{j=1}^{n} F_{ij} = 1 \quad (3)$$

where:

| | |
|---|---|
| $F_{ij}$ | Surface $i$-to-surface $j$ (including ambient and surface $i$ itself, if applicable) view factor, dimensionless. |

However, this is clearly not the case for industrial cells. Consider, for example, the hot sidewall item 3 shown in Figure 7, Left: even though there is no direct line of sight between item 3 and item 1, items 4, 6, 7 and 8 are in its field of vision and, as a consequence, $F_{3amb} < 1$.

### 2.1 Radiation Resistances Network: the 3-surfaces Enclosure Problem

A slightly better representation of the net radiation heat losses between the potshell and the ambient can be obtained by the classical 3-surfaces enclosure problem, depicted in Figure 8 by means of a network of thermal radiation resistances. The system may be solved by means of Kirchoff's Law at each individual node $J_i$ while assuming uniform temperatures $T_i$. Once all $J_i$ are known, individual net radiative heat losses can be derived by Equation (4).

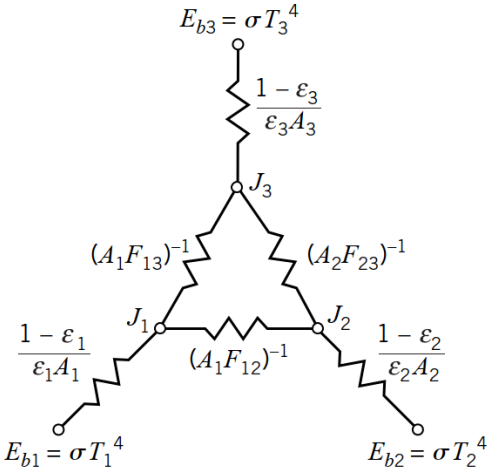


**Figure 8. Thermal radiation resistances network for 3-surfaces enclosure problem – adapted from [17].**

where:

| | |
|---|---|
| $A_i$ | Surface area $i$, m$^2$ |
| $E_{bi}$ | Black body emission at surface $i$, W/m$^2$ |
| $J_i$ | Radiosity (*i.e.*, the sum of direct emission and reflected irradiation) at real surface $i$, W/m$^2$. |

The $\left(\frac{1-\varepsilon_i}{A_i \cdot \varepsilon_i}\right)$ terms in Figure 8 are known as "surface resistances" and describe the transition from a black body behavior (*i.e.*, a perfect radiation emitter/absorber) to that of a real surface, capable of reflecting a portion of incident radiation. The $\left(A_i \cdot F_{ij}\right)^{-1}$ terms are called "space resistances" and describe the interaction between the different gray surfaces in the system by means of their individual view factors $F_{ij}$.

$$q_{rad,i} = (E_{bi} - J_i) \cdot \left(\frac{A_i \cdot \varepsilon_i}{1-\varepsilon_i}\right) \tag{4}$$

where:

| | |
|---|---|
| $q_{rad,i}$ | Net radiation heat losses at surface $i$, W. |

*Application Example*

Consider hypothetical *in-situ* measurements revealing that the doubly symmetric hot sidewall segment from Figure 7, Left, loses $q_{rad,sym}$ = 2051 W by means of thermal radiation to its surroundings (or $q_{rad,full}$ = 8204 W for the full enclosure). Based on the data found in Table 1 and Table 2, (1) calibrate $T_{rad,amb}$ and then (2) estimate net radiation heat losses at $T_{hot\ sidewall}$ = 500 °C for both 2-surfaces and 3-surfaces enclosures.

**Table 1. Analytical calculation parameters for 2-surfaces (hot sidewall-ambient) enclosure.**

| Parameter \| Surface | 1 | 2 |
|---|---|---|
| Description | Hot sidewall (refer to item 3 from Figure 7, Left) | Ambient |
| $\varepsilon$, [-] | 0.85 | 1.00 |
| $T$, [°C] | 350 | To be calibrated |
| $A$, [m$^2$] | | |
| *Double symmetry enclosure** | 0.318 | ∞ |
| *Full enclosure* | 1.272 | ∞ |
| $F_{1j}$, [-] | | |
| *Full enclosure* | – | 1.000 |
| $F_{2j}$, [-] | Computed by means of the reciprocity rule, $A_i \cdot F_{ij} = A_j \cdot F_{ji}$ | |

** For a double symmetry enclosure, $A_i$ is reported for the independent segments only, which amounts to 25 % of the full enclosure.*

**Table 2. Analytical calculation parameters for 3-surfaces (hot sidewall-ambient-cradles and other shell segments) enclosure.**

| Parameter \| Surface | 1 | 2 | 3 |
|---|---|---|---|
| Description | Hot sidewall (refer to item 3 from Figure 7, Left) | Ambient | All other potshell segments (refer to Figure 7, Left) |
| $\varepsilon$, [-] | 0.85 | 1.00 | 0.85 |
| $T$, [°C] | 350 | To be calibrated | 127 |
| $A$, [m$^2$] | | | |
| *Double symmetry enclosure** | 0.318 | ∞ | 4.306 |
| *Full enclosure*** | 1.272 | ∞ | 17.224 |
| $F_{1j}$, [-] | | | |
| *Full enclosure* | – | 0.460 | 0.540 |
| $F_{2j}$, [-] | Computed by means of the reciprocity rule, $A_i \cdot F_{ij} = A_j \cdot F_{ji}$ | | |
| $F_{3j}$, [-] | | | |
| *Full enclosure*** | 0.040 | 0.960 | – |

** For a double symmetry enclosure, $A_i$ is reported for the independent segments only, which amounts to 25 % of the full enclosure.*

*** The radiosity method requires the employment of $q_{rad}$, $A_i$ and $F_{ij}$ for the full enclosure in order to ensure the energy balance.*

The ambient radiative temperature for the 2-surfaces (hot sidewall-ambient) enclosure, $T_{rad,amb\_2surf}$, is given by Equation (5):

$$T_{rad,amb\_2surf} = \left[{T_1}^4 - \left(\frac{q_{rad,full}}{A_1 \cdot F_{12} \cdot \varepsilon_1 \cdot \sigma}\right)\right]^{1/4} = 360.73 \text{ K} = 87.58 \text{ °C} \quad (5)$$

The ambient radiative temperature for the 3-surfaces (hot sidewall-ambient-other shell segments) system is obtained by means of the radiosity method (see Figure 8), which yields $T_{rad,amb\_3surf}$ = 306.45 K = 33.30 °C, significantly lower than $T_{rad,amb\_2surf}$.

With $T_{rad,amb\_2surf}$ and $T_{rad,amb\_3surf}$ calibrated, new net radiation heat losses at $T_{hot\ sidewall}$ = 500 °C can be then computed:

- Double symmetry 2-surfaces enclosure: $q_{rad,sym\_2surf}$ = 5216 W
- Double symmetry 3-surfaces enclosure: $q_{rad,sym\_3surf}$ = 5207 W.

The small difference $\Delta q_{rad}$ = 9 W in the predictions above stems from the fact that the potshell is a gray surface and, as such, it reflects a portion of all incident irradiation. The low reflectivity of rusted carbon steel, *i.e.,* $(1 - \varepsilon_{potshell})$ = 15 %, is what enables the use of the traditional $h_{eqv,i} = h_{conv,i} + h_{rad,i}$ approach for the energy balance of Hall-Héroult cells – Equation (2).

Notice, however, that $\Delta q_{rad}$ increases as emissivity $\varepsilon_i$ decreases. In order to properly handle the relatively low emissivity 0.4 < $\varepsilon_{busbar}$ < 0.5 of aluminium busbars (such as items 12 and 13 from Figure 7, Right), the radiosity method was implemented in the modernized ANSYS-based TE model previously published by the authors [1–3]. Other features (such as neighboring potshells and pot-to-pot slabs) can be included in the TE analyses as needed. Albeit more computationally expensive, the radiosity method offers the additional advantage of (ideally) requiring the calibration of a single $T_{rad,amb}$ for the entire radiation enclosure as opposed to one per potshell segment, as it is commonly the case for the traditional $h_{eqv,i} = h_{conv,i} + h_{rad,i}$ approach.

## 3. Implementation in the Modernized TE Finite Element (FE) Model

The authors introduced in 2020 a modernized ANSYS-based TE model [1] that builds upon the foundations first introduced and further developed by Dupuis [4–8] from the mid-1980s up to his most recent publications in the 2020s. The prediction of the ledge profile is achieved by means of successive repositioning of the solidification front to solve the Stefan problem. In 2021, a simplified approach for the prediction of the ledge trench (Figure 6) was introduced [2] as well as the capability of considering different bath chemistries, solidification temperatures and superheats for each region of the ledge. In 2023, the modeling platform was expanded to add half and full cell geometries as well as the possibility of accounting for the impact of the metal heave profile (Figure 4).

In the present work, a great deal of care was taken to ensure the robustness and accuracy of the overall solution. To achieve this, of a series of user routines were developed to leverage the ANSYS built-in radiosity solver in tandem with the conventional TE diffusion model at the core of the cell energy balance platform. The new routines:

- Automatically generate the radiosity surface loads on applicable areas and generate the corresponding surface effect elements;
- Automatically assign (or remove) those elements to (or from) the corresponding cathodic or anodic portions of the cell control volume boundaries in order to properly account for energy losses;
- Efficiently exploit the symmetrical nature of the view factor matrix whenever applicable in order to reduce total elapsed computational time;
- Ensure the consistency of the view factor matrix by enforcing compliance with the reciprocity rule, $A_i \cdot F_{ij} = A_j \cdot F_{ji}$;
- Automatically assess and report errors on both the radiosity model energy balance and view factor reciprocity rule for all defined radiation surfaces of each enclosure.

It is worth pointing out that several of those advanced radiosity solver features are not readily available from the graphical user interface.

## 4. Numerical Experiments

To illustrate the potential applications of the integrated TE diffusion-radiosity model, a series of analyses were performed according to the following:

- Complete pot slice geometry where both the ledge profile and cell energy balance are simultaneously converged. All main process and heat transfer parameters as per [3];
- Distinct chemical compositions for the upper (facing bath) and lower (facing metal) portions of the ledge with enhanced heat transfer at the ledge trench;
- Flat metal pad-bath interface;
- Uniform cathodic and anodic current distributions;
- Double symmetry radiation enclosures as per Figure 7;
- When present, the (600 × 100) mm$^2$ busbars are excluded from the cell heat balance control volume and only the surfaces facing the potshell are explicitly represented, as per Figure 9 (where view factors are expressed in % varying from 0 to 100 %);
- For the sake of simplification, busbars surfaces are held at a uniform temperature $T_{busbar}$:
    - A more comprehensive description of the problem would account for the prediction of $T_{busbar}$ while including Joule Effect and heat exchange with both the reduction cell and its surroundings. The prediction of $T_{busbar}$ is, however, excluded from the present work;
- Potshell emissivity $\varepsilon_{potshell}$ = 0.85, and cathode ring busbar emissivity $\varepsilon_{busbar}$ = 0.40;
- Potshell and cathode ring busbars meshed with 25 mm linear elements;
- Reported average hot sidewall temperatures are evaluated over a line above the collector bars, as per Figure 7, Left.

Table 3 describes the different test cases studied in the present work.

**Table 3. Description of test cases.**

| Case # | Description | Topology |
|---|---|---|
| 1 | TE diffusion model only;<br>Traditional equivalent heat transfer coefficient $h_{eqv,i} = h_{conv,i} + h_{rad,i}$ approach;<br>Radiative losses to ambient only, $F_{iamb}$ = 1 (full enclosure);<br>Each potshell surface is subjected to a given $T_{rad,amb}$, based on a previous model setup.<br>*(Reference case)* | Figure 9, Top Left |
| 2 | Integrated radiosity-TE diffusion model;<br>Convection heat transfer coefficient $h_{eqv,i} = h_{conv,i}$ only and surface-to-surface radiation;<br>Individual radiation surfaces assigned to different enclosures (notice that the view factor between different segments is necessarily equal to zero);<br>Radiative losses to ambient only, $F_{iamb}$ = 1 (full enclosure);<br>Each potshell surface is subjected to a given $T_{rad,amb}$, as per Case 1 (the objective of this analysis is to reproduce the behavior of Case 1 while taking the radiosity model into account).<br>*(Integrated radiosity-TE diffusion model implementation)* | |
| 3 | Integrated radiosity-TE diffusion model;<br>Convection heat transfer coefficient $h_{eqv,i} = h_{conv,i}$ only and surface-to-surface radiation;<br>All radiation surfaces within the same enclosure; | |

| | | |
|---|---|---|
| | Radiative heat exchange between potshell segments themselves and ambient, $F_{iamb}$ < 1 (full enclosure);<br>$T_{rad,amb}$ = 33.3 °C.<br>*(Impact of rigorous view factor calculation on potshell heat losses and TE model calibration)* | |
| 4 | Integrated radiosity-TE diffusion model;<br>Convection heat transfer coefficient $h_{eqv,i} = h_{conv,i}$ only and surface-to-surface radiation;<br>All radiation surfaces within the same enclosure;<br>Radiative heat exchange between potshell segments themselves, cathode ring busbar and ambient, $F_{iamb}$ < 1 (full enclosure);<br>$T_{rad,amb}$ = 33.3 °C;<br>Prescribed busbar temperatures, 70 °C ≤ $T_{busbar}$ ≤ 200 °C.<br>*(Impact of cathode ring busbars at different elevations and prescribed $T_{busbar}$ on potshell temperature)* | Figure 9, Top Right |
| 5 | | Figure 9, Bottom Left |
| 6 | | Figure 9, Bottom Right |

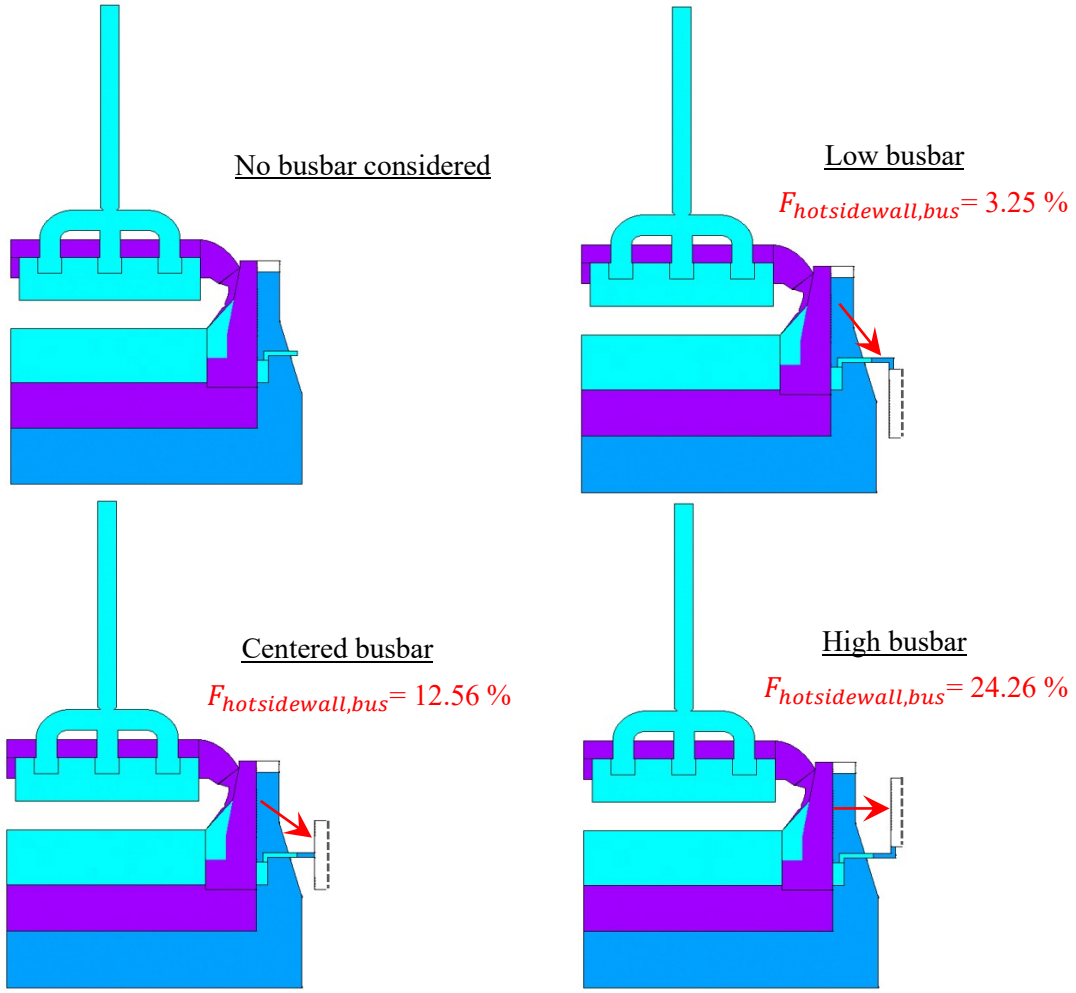


**Figure 9. Complete cell slice geometries with or without cathode ring busbars, where the red arrow represents the hot sidewall-to-busbars direct line-of-view and relevant average view factors are reported for the full enclosure. Top Left: typical cell slice only. Top Right: typical cell slice and low busbar. Bottom Left: typical cell slice and mid-height busbar. Bottom Right: typical cell slice and high busbar.**

### 4.1 Results

Table 4 presents the main energy balance results for all analyses. Notice that results for Cases 4–6 were computed at uniform $T_{busbar}$.= 135 °C.

**Table 4. Main energy balance results.**

| Result | Case 1 | Case 2 | Case 3 | Case 4 | Case 5 | Case 6 |
|---|---|---|---|---|---|---|
| Bulk bath temperature, $T_{opr}$, [ºC] | 976.17 | 976.20 | 976.81 | 976.85 | 976.90 | 976.97 |
| Liquidus temperature evaluated at bulk bath composition, $T_{liq}$, [ºC] | 967.99 | 967.99 | 967.99 | 967.99 | 967.99 | 967.99 |
| Bath superheat, $\Delta T_{upper}$, [ºC] | 8.18 | 8.20 | 8.82 | 8.86 | 8.91 | 8.98 |
| Bulk metal pad temperature, $T_{alu}$, [ºC] | 972.17 | 972.20 | 972.81 | 972.85 | 972.90 | 972.97 |
| Eutectic point evaluated at bath film composition, $T_{eut}$, [ºC] | 956.46 | 956.46 | 956.46 | 956.46 | 956.46 | 956.46 |
| Metal pad superheat, $\Delta T_{lower}$, [ºC] | 15.71 | 15.74 | 16.35 | 16.39 | 16.44 | 16.51 |
| Cell internal heat, [kW] | 829.38 | 829.42 | 831.73 | 831.95 | 832.02 | 832.09 |
| Anode heat losses, [kW] | 263.33 | 263.59 | 265.69 | 265.78 | 265.98 | 266.28 |
| Cathode heat losses, [kW] | 566.40 | 566.12 | 566.09 | 566.18 | 566.06 | 565.81 |
| *Bath-to-upper ledge heat losses* | 84.39 | 84.77 | 92.34 | 92.75 | 93.45 | 94.33 |
| *Liquids-to-trench heat losses* | 30.15 | 30.26 | 32.77 | 32.92 | 33.10 | 33.33 |
| *Metal pad-to-lower ledge heat losses* | 220.42 | 220.92 | 211.17 | 211.86 | 212.80 | 213.17 |
| *Metal pad-to-cathode panel heat losses* | 76.05 | 75.00 | 74.36 | 72.97 | 71.22 | 69.76 |
| Total cell heat losses, [kW] | 829.73 | 829.72 | 831.78 | 831.96 | 832.03 | 832.09 |
| Anode voltage drop, [mV] | 426.82 | 426.82 | 426.81 | 426.81 | 426.81 | 426.81 |
| Cathode voltage drop, [mV] | 338.45 | 338.58 | 345.21 | 345.83 | 346.05 | 346.28 |
| Cell heat imbalance, [kW] | -0.35 | -0.30 | -0.01 | -0.01 | -0.01 | 0.01 |
| Ledge RMS temperature norm*, **, [ºC] | 0.21 | 0.20 | 0.24 | 0.21 | 0.24 | 0.23 |
| Ledge INFINITE temperature norm**, ***, [ºC] | 0.61 | 0.60 | 0.55 | 0.43 | 0.50 | 0.48 |

** Refers to the root mean square difference computed with the local ledge melting temperature for all eligible nodes at the ledge-liquids interface.*
*** All nodes where the ledge is locally melted (*i.e.*, switched to liquid aluminum) are excluded from error assessment.*
**** Refers to the maximum absolute computed difference with the local ledge melting temperature for an individual eligible node at the ledge-liquids interface.*

#### 4.1.1 Case 2: Integrated Radiosity-TE Diffusion Model Implementation

Case 2 is meant to replicate the Case 1 behavior by means of the integrated radiosity-TE diffusion model. Each radiation surface was therefore assigned to a unique enclosure, such that only radiative heat losses to the ambient are possible (*i.e.*, $F_{iamb}$ = 1 for full enclosure).

As expected, both approaches yield virtually identical results, both in terms of main energy balance parameters – Table 4 – and ledge profile – Figure 10. Notice that the small observed differences are attributed to the different convergence strategies applicable to each method.

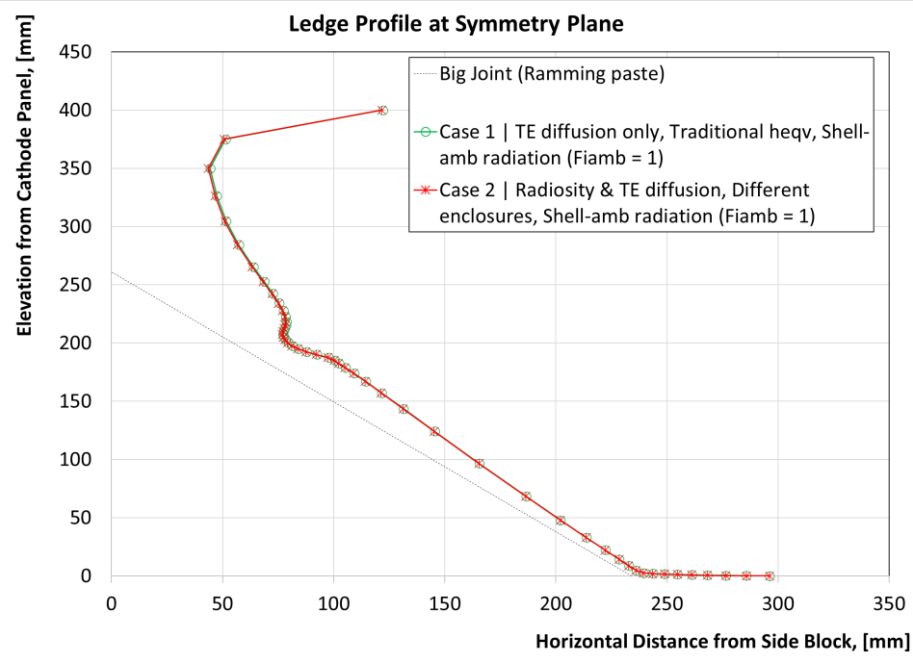


**Figure 10. Predicted ledge profile for Cases 1 and 2**

Potshell temperature profile for Case 1 is seen in Figure 11, Left, where the averaged reported $T_{hot\ sidewall,avg}$ value is evaluated along the path identified by the black dotted line (also shown in Figure 7, Left). Furthermore, notice that Case 2 yields a similar potshell temperature distribution and is omitted in this work to avoid repetition.

Based on the above results, it is concluded that the radiosity method was successfully implemented into the existing cell energy balance platform.

### 4.1.2 Case 3: Impact of Rigorous View Factor Calculation on Potshell Heat Losses and TE Model Calibration

Next, the impact of rigorous computation of view factors on potshell heat losses was studied by assigning all the radiation surfaces to a single enclosure. Since potshell segments can now exchange heat by radiation with each other as per Figure 7, it follows that their view factor with respect to ambient is not necessarily $F_{iamb}$ = 1 (for full enclosure). This means that not only their overall resistance to radiative heat transfer is modified, but also the proportion by which heat is exchanged between different surfaces (including ambient) within the enclosure, according to Figure 8.

Figure 11 compares the typical potshell temperature profiles for Cases 1 and 3. As expected, reducing pot-shell-to-ambient view factor effectively acts as an “additional thermal insulation” to radiative cathode heat losses and a substantial increase (about 39 °C) in the hot sidewall temperature is observed with respect to the reference case.

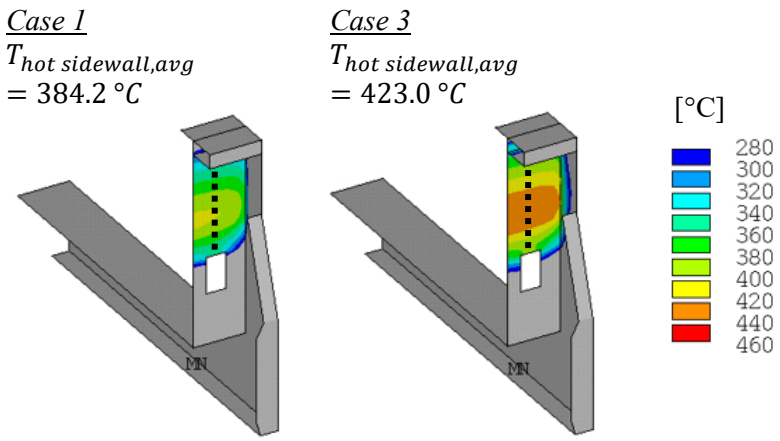


**Figure 11. Potshell temperature distribution (averaged reported value is evaluated along the black dotted line). Left: Case 1. Right: Case 3.**

This is followed by a 0.6 °C increase in bath superheat, as seen in Table 4, which leads to a thinner ledge (and a shorter ledge toe) when compared to that of Case 1, Figure 12. The observed differences in predictions indicate that the original set of $T_{rad,amb}$ individually calibrated for each potshell segment from Case 1 is not applicable anymore when $F_{iamb} \neq 1$.

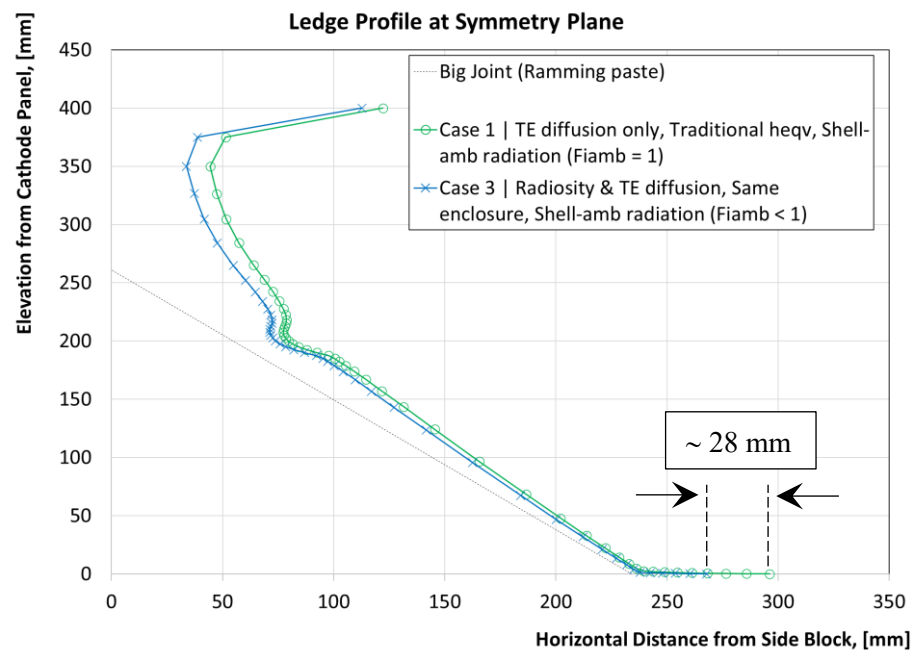


**Figure 12. Predicted ledge profile for Cases 1 and 3.**

As previously discussed in Section 2.1, adequate calibration parameters can be obtained for both $h_{eqv,i}$ and radiosity approaches, in such a way that both calculation strategies yield similar results. For instance, the equivalent heat transfer coefficients $h_{eqv,i}$ of Case 1 can be adjusted to provide a potshell temperature distribution comparable to that of Case 3 even though the interaction of different shell segments is not explicitly accounted for – see Figure 13.

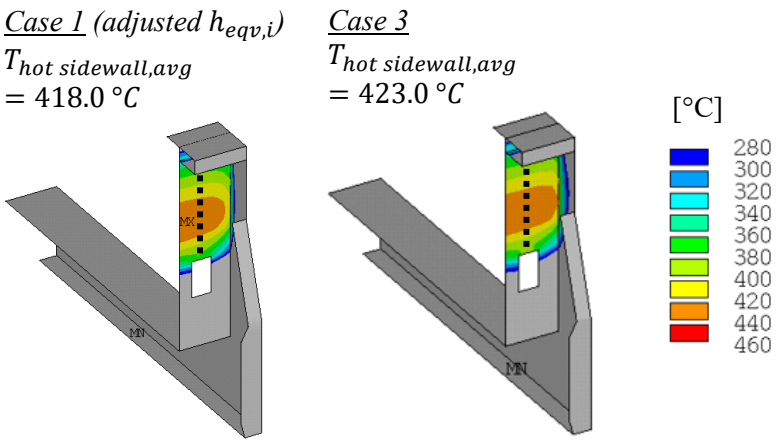


**Figure 13. Potshell temperature distribution (averaged reported value is evaluated along the black dotted line). Left: Case 1 with adjusted equivalent heat transfer coefficients $h_{eqv,i}$. Right: Case 3.**

It is worth stressing that the integrated radiosity-TE diffusion model simplifies the model calibration effort by providing an inherently more accurate description of both (1) radiation resistances and (2) radiative environment, as the view factors and temperature of all potshell segments are explicitly accounted for in the calculation. As such, the radiosity method (ideally) requires the calibration of only one parameter, namely, a single $T_{rad,amb}$ for the entire enclosure (as opposed to several unique ones).

It must be stressed, however, that both geometric setup and boundary conditions definition for the integrated radiosity-TE diffusion model is inherently more complex than that of the traditional equivalent heat transfer coefficient approach. It should also be noticed that integrated radiosity-TE diffusion model is inherently more computationally expensive than the traditional $h_{eqv,i} = h_{conv,i} + h_{rad,i}$ method.

### 4.1.3 Cases 4–6: Impact of Cathode Ring Busbars at Different Elevations and Prescribed $T_{busbar}$ on Potshell Temperature)

The impact of the cathode ring busbars at prescribed $T_{busbar}$ on the potshell temperature distribution was studied for a 600 mm tall busbar located at different heights, and therefore, having different view factors with respect to the hot sidewall – refer to Figure 9, Top Right, Bottom Left and Bottom Right. It must be noticed once more that a more comprehensive description of this system would account for the prediction of $T_{busbar}$, which is excluded from the present work for the sake of simplification.

Figure 14 compares the typical potshell temperature profiles while considering $T_{busbar}$ = 135 °C for Cases 4 through 6 where it can be seen that the sidewall temperature consistently increases with busbar height as the view factor between potshell and ambient becomes increasingly reduced (*i.e.*, the potshell becomes "more insulated"), consistent with Section 4.1.2. This is followed by small increases in bath superheat, as seen in Table 4, and therefore, small reductions in ledge thickness, Figure 15.

When appreciated in tandem, the temperature distributions from both Figure 11 and Figure 14 clearly highlight the strong dependence of potshell radiative heat losses on the accurate description of view factors.

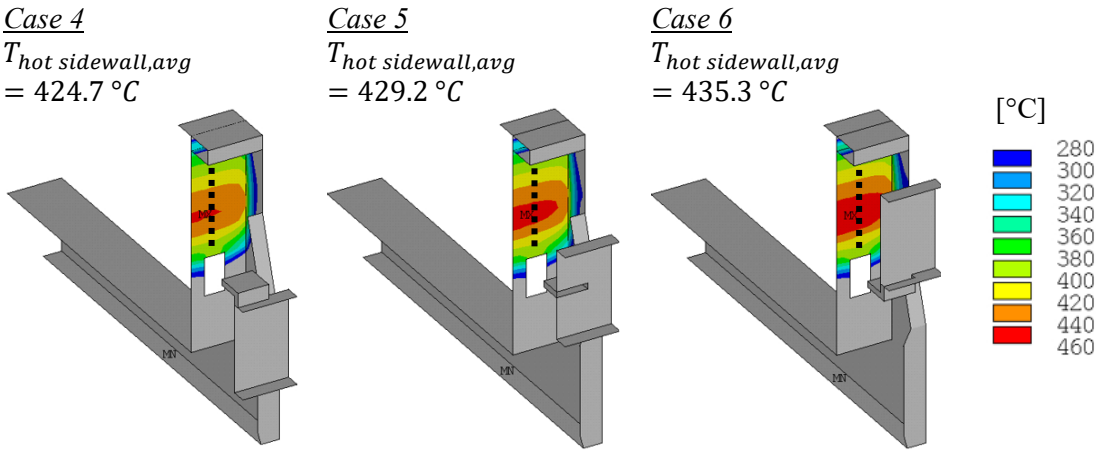


**Figure 14. Potshell temperature distribution, where all busbar segments were held at $T_{busbar}$ = 135 °C (averaged reported value is evaluated along the black dotted line). Left: Case 4. Center: Case 5. Right: Case 6.**

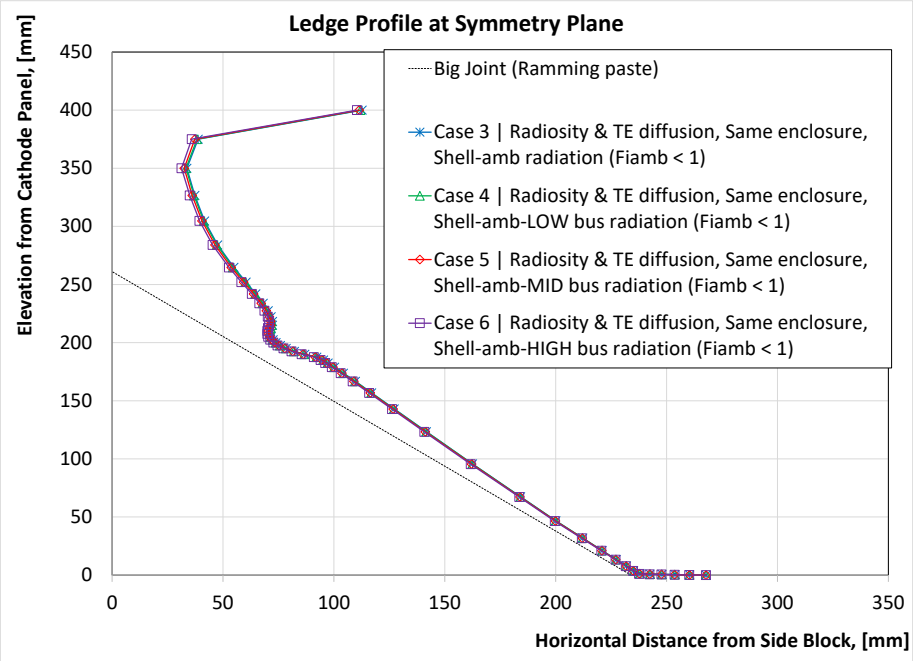


**Figure 15. Predicted ledge profile for Cases 3–6.**

As expected, the impact of varying busbar temperature $T_{busbar}$ on hot sidewall average temperature $T_{hot\ sidewall,avg}$ was also found to become increasingly important as the hot sidewall-to-busbars view factor $F_{hotsidewall,bus}$ increases or, conversely, as hot sidewall-to-ambient view factor $F_{potshell,amb}$ decreases, as per Table 5.

At the worst of cases, the hot sidewall average temperature $T_{hot\ sidewall,avg}$ is expected to result in a $\left(\frac{\Delta T_{hot\ sidewall,avg}}{\Delta T_{busbar}}\right)_{Highbusbar}$ $\times$ (200 °C – 140 °C) = 1.7 °C difference only between US and DS sidewalls, if the pot-to-pot busbar circuit found in Figure 5 were to be installed facing the liquid phases, similar to that of Figure 9, Top Right.

**Table 5. Impact of cathode ring busbar temperature $T_{busbar}$ on average hot sidewall temperature $T_{hot\ sidewall,avg}$ for different configurations – refer to Figure 9.**

| Case # | Busbar Position | Hot sidewall-to-Ambient View Factor, [-], (full enclosure) | Hot sidewall average temperature, [°C], for Varying Uniform Busbar Temperature | | | $\left(\frac{\Delta T_{hot\ sidewall,avg}}{\Delta T_{busbar}}\right)$ |
|---|---|---|---|---|---|---|
| | | | $T_{busbar}$ = 70 °C | $T_{busbar}$ = 135 °C | $T_{busbar}$ = 200 °C | |
| 3 | – | 46.07 % | 423.0 | | | – |
| 4 | Low | 42.82 % | 424.2 | 424.7 | 425.4 | 0.92E-2 °C/°C |
| 5 | Mid-height | 33.51 % | 428.3 | 429.2 | 430.7 | 1.85E-2 °C/°C |
| 6 | High | 21.81 % | 434.0 | 435.3 | 437.6 | 2.77E-2 °C/°C |

## 5. Conclusion

The radiosity method was successfully integrated to the existing TE cell energy balance platform by means of a series of user routines leveraging the ANSYS built-in radiosity solver while ensuring the consistency of the results. The implementation of the integrated radiosity-TE diffusion model was validated by directly comparing its results to those yielded by the traditional equivalent heat transfer coefficient $h_{eqv,i} = h_{conv,i} + h_{rad,i}$ approach, commonly used in the TE design and assessment of Hall-Héroult cells.

It was found that the rigorous computation of individual $F_{ij}$ view factors leads to higher hot sidewall average temperature, bath superheat and thinner side ledges when compared to those obtained for the traditional approach if the same set of calibration parameters is considered. This indicates that different model calibrations are required, depending on the chosen modeling approach.

While the traditional $h_{eqv,i}$ method is valid and can be used if properly calibrated with measurements, TE model calibration tends to be simplified when a rigorous formulation of the radiation heat transfer phenomenon is considered given its inherently better description of both (1) radiation resistances and (2) radiative environment. As such, the radiosity method (ideally) requires the calibration of only one parameter, namely, a single $T_{rad,amb}$ for the entire enclosure (as opposed to several unique ones). It is also worth noticing that several distinct geometric features can be accounted for in the integrated radiosity-TE diffusion model, such as complete pot-to-pot circuits, pot-to-pot slabs, potroom infrastructure and adjacent potshells, as needed.

It must be stressed, however, that both geometric setup and boundary conditions definition for the integrated radiosity-TE diffusion model is inherently more complex than that of the traditional equivalent heat transfer coefficient approach. It should also be noticed that integrated radiosity-TE diffusion model is inherently more computationally expensive than the traditional $h_{eqv,i} = h_{conv,i} + h_{rad,i}$ method.

Finally, numerical predictions suggest that the hot sidewall segment average temperature (facing liquids, refer to item 3 in Figure 7) is weakly influenced (< 5 °C) by the US-to-DS differences in busbar temperature commonly found in Hall-Héroult cells. As expected, the hot sidewall segment average temperature also varies with cathode busbar ring height as $F_{potshell,amb}$ becomes increasingly reduced (*i.e.*, the potshell becomes "more insulated"). Calculations in the present

work estimated an impact of about 10 °C in $T_{hot\ sidewall,avg}$, suggesting that the influence of the hot sidewall-to-busbar view factor $F_{hotsidewall,bus}$ is more relevant than that of busbar temperature $T_{busbar}$ itself.

## 6. References


1. Daniel Richard et al., A modernized ANSYS-based finite element model for the thermal-electrical design of aluminum reduction cells, *Proceedings of the 38th International ICSOBA Conference*, Virtual Event, 16–18 November, 2020, Paper AL03, *Travaux* 49, 563–580.
2. André Felipe Schneider et al., A Thermoelectrical approach for the modelling of different ledge regions in aluminum reduction cells, *Proceedings of the 39th International ICSOBA Conference*, Virtual Event, 22–24 November, 2021, Paper AL20, *Travaux* 50, 835–853.
3. André Felipe Schneider et al., Impact of Metal Pad Heave on Shell Temperature of Aluminum Reduction Cells, *Proceedings of the 41st International ICSOBA Conference*, Dubai, United Arab Emirates, 06–09 November, 2023, Paper AL49, *Travaux* 52, 1725–1740.
4. Marc Dupuis and Imad Tabsh, Thermo-electric coupled field analysis of aluminium reduction cells using the ANSYS parametric design language, *Proceedings of the ANSYS Fifth International Conference*, Vol 3, 1991, 1780–1792.
5. Marc Dupuis, Thermo-electric design of a 400 kA cell using mathematical models: a tutorial, *Light Metals* 2000, 297–302.
6. Marc Dupuis, Computation of aluminium reduction cell energy balance using ANSYS® finite element models, *Light Metals* 1998, 409–417.
7. Marc Dupuis, Computation of accurate horizontal current density in metal pad using a full quarter cell thermo-electric model, *Proceedings of CIM* 2001, 3–11.
8. Marc Dupuis, How to limit the heat loss of anode stubs and cathode collector bars in order to reduce cell energy consumption, *Light Metals* 2019, 521–531.
9. Steeve Renaudier et al., Alucell: a unique suite of models to optimize pot design and performance, *Light Metals* 2018, 541–549.
10. S. Langlois et al., 3D coupled and thermo-electrical modelling applied to AP Technology pots, *Light Metals* 2015, 771–775.
11. Pascal Thibeault et al., AP44 development at Alma, *Light Metals* 2018, 737–744.
12. Louis Bugnion and René von Kaenel, Impact of TE-MHD Coupling on Cell Performance, *Proceedings of the 41st International ICSOBA Conference*, Dubai, United Arab Emirates, 06–09 November, 2023, Paper AL50, *Travaux* 52, 1741–1747.
13. Nadia Chailly et al., Alucell latest development: modelling impact of CO2 bubbles and anode slot configuration on liquid flows in Hall-Héroult pot, *Proceedings of the 41st International ICSOBA Conference*, Dubai, United Arab Emirates, 06–09 November, 2023, Paper AL22, *Travaux* 52, 1439–1452.
14. Vishal Ahmad et al., Amperage increase program and enablers in EGA Al Taweelah DX technology potlines, *Light Metals* 2024, 520–525.
15. Nick Depree et al., The "virtual battery" – operating an aluminium smelter with flexible energy input, *Light Metals* 2016, 571–576.
16. Zhou Sen et al., Controlled ledge profile of aluminum smelting cell using sidewalls heat exchangers supplied with molten salt, *Journal of Sustainable Metallurgy*, Vol. 9, (2023), 550-563.
17. Frank P. Incropera, David P. Dewitt et al., *Fundamentals of heat and mass transfer*, 6th Edition, Hoboken, John Wiley & Sons, 2007, 997 pages.